A new twist on bacterial motility – two distinct type IV pili revealed by cryoEM

Alexander Neuhaus[1,2], Muniyandi Selvaraj[3,-], Ralf Salzer[4,X], Julian D. Langer[5,6], Kerstin Kruse[4], Kelly Sanders[1,2], Bertram Daum[1,2], Beate Averhoff[4] and Vicki A. M. Gold[1,2,#],

[1] Living Systems Institute, University of Exeter, Stocker Road, EX4 4QD, United Kingdom

[2] College of Life and Environmental Sciences, Geoffrey Pope, University of Exeter, Stocker Road, Exeter, EX4 4QD, United Kingdom

[3] Department of Structural Biology, Max Planck Institute of Biophysics, Max-von-Laue Str. 3, 60438 Frankfurt am Main, Germany

- Current address: Laboratory of Structural Biology, Helsinki Institute of Life Science, 00014 University of Helsinki, Finland

[4] Molecular Microbiology and Bioenergetics, Institute of Molecular Biosciences, Goethe University Frankfurt, Max-von-Laue Str. 9, 60438 Frankfurt am Main, Germany

[X] Current address: Structural Studies Division, Medical Research Council – Laboratory of Molecular Biology, Cambridge Biomedical Campus, Francis Crick Ave, Cambridge CB2 0QH, United Kingdom

[5] Department of Molecular Membrane Biology, Max Planck Institute of Biophysics, Max-von-Laue Str. 3, 60438 Frankfurt am Main, Germany

[6] Proteomics, Max Planck Institute for Brain Research, Max-von-Laue Str. 4, 60438 Frankfurt am Main, Germany

[#]corresponding author

Keywords: Type IV pili, electron cryo-tomography, electron cryo-microscopy, helical reconstruction, pilin, flexible filaments

Summary

Many bacteria express flexible protein filaments on their surface that enable a variety of important cellular functions. Type IV pili are examples of such filaments and are comprised of a helical assembly of repeating pilin subunits. Type IV pili are involved in motility (twitching), surface adhesion, biofilm formation and DNA uptake (natural transformation). They are therefore powerful structures that enable bacterial proliferation and genetic adaptation, potentially leading to the development of pathogenicity and antibiotic resistance. They are also targets for drug development.

By a complement of experimental approaches, we show that the bacterium *Thermus thermophilus* produces two different forms of type IV pilus. We have determined the structures of both and built atomic models. The structures answer key unresolved questions regarding the molecular architecture of type IV pili and identify a new type of pilin. We also delineate the roles of the two filaments in promoting twitching and natural transformation.

41 **Main**

42 Type IV pili (T4P) are flexible extracellular protein filaments found on many bacteria. They
43 form multifunctional fibres involved in twitching motility, adhesion, immune evasion,
44 bacteriophage infection, virulence and colony formation. T4P have also been linked to DNA
45 uptake, called natural transformation, which is a powerful mechanism that enables genetic
46 adaptation [1–3]. The filaments are homopolymers composed of thousands of pilin subunits,
47 which form helical arrays measuring several micrometres in length. How T4P are involved in
48 seemingly unrelated functions such as motility and natural transformation is so far unclear.
49

50 Depending on the bacterial species, pilins range from 90 to 250 amino acids in length. They
51 are produced as prepilins with a typical class III signal peptide [4,5]. The preprotein is
52 translocated via the Sec pathway into the cell membrane where the signal peptide is cleaved
53 by prepilin peptidase, priming the pilin for incorporation into the growing pilus. Filament
54 assembly is ATP-dependent and occurs at an inner membrane platform which contains PilC,
55 PilM, PilN and PilO [6]. In *Thermus thermophilus,* assembly of pilins into a T4P filament depends
56 on the assembly ATPase PilF, which interacts with the inner membrane platform via PilM [7].
57 Two retraction ATPases, PilT1 and PilT2, are essential for T4P depolymerisation [8,9]. T4P are
58 extruded by the outer membrane secretin PilQ [10–13]. Recently, it has been suggested that
59 expression of the *T. thermophilus* major pilin PilA4 is temperature dependent, leading to
60 hyperpiliation at suboptimal growth temperatures [14]. The first two *in situ* structures of T4P
61 assembly machineries were solved only recently in both open (pilus assembled) and closed
62 (pilus retracted) states [11,15], yet detailed information regarding the molecular interactions
63 governing filament assembly was lacking.
64

65 Crystal structures of full length pilins or head domains from various bacteria are available
66 in different oligomeric states [6,16–22]. Pilins have a conserved N-terminal α-helix, with a 4-5
67 stranded anti-parallel β-sheet at the C-terminus. The α-helix forms the core of the filament,
68 while the globular β-sheet head domain is solvent exposed and subject to post-translational
69 modifications [16,17]. To date, five low-resolution electron cryo-microscopy (cryoEM) structures
70 of isolated T4P have been reported. The first, a 12.5 Å structure from *Neisseria gonorrhoeae*,
71 was sufficient to place crystal structures of pilins into the data but not to resolve their
72 structure within the map [17]. Four subsequent structures from *Pseudomonas aeruginosa*, two
73 *Neisseria* species and enterohemorrhagic *Escherichia coli* have been determined in the 5-8 Å
74 resolution range [23–25].

In this study, we combine different modes of cryoEM: electron cryo-tomography (cryoET) and single-particle cryoEM, with functional data to study the T4P of *T. thermophilus,* which is a well-established model organism. Surprisingly, we detect two forms of T4P, a wider and a narrower form, assembled through the same machinery. We determine structures of the two filaments at so-far unprecedented resolution (3.2 Å and 3.5 Å, respectively). This has enabled us to visualise near atomic-level detail and build atomic models for each filament *ab initio*. Our data unambiguously demonstrate that the wider pilus is composed of the major pilin PilA4. Proteomics and knock-out mutants reveal that the narrow pilus consists of a previously unknown pilin, which we name PilA5. Functional experiments confirm that PilA4 is involved in natural transformation whereas PilA5 is essential for twitching motility [26]. Our results shed new light on bacterial motility and gene transfer, and will help to guide the development of new drugs to fight microbial pathogens.

Two types of T4P are assembled from the same machinery

Cells of *T. thermophilus* strain HB27 assemble T4P pili on their surface [27] , predominantly at the cell poles [11]. Performing cryoET on cells grown at the optimal growth temperature of 68 °C revealed two types of pilus, with differences in their diameter. They emerge from the same assembly machinery (Fig. 1a, b), suggesting that they are both T4P. We have previously shown that transcription of the major pilin gene, *pilA4*, is upregulated at low temperature [14]. To address the question of whether the growth temperature affects the assembly of the two forms of pilus, we analysed the pili emerging from cells grown at the sub-optimal growth temperature of 58 °C by cryoET. Again, two types of pilus were observed (Fig. 1c, d). Pili emerge from T4P complexes only sporadically [11], thus filaments were isolated from cells in order to investigate their structure in more detail. Both wide and narrow forms of the filament were detected in these preparations (Fig. S1a-d).

To investigate the composition of the two pilus forms, we performed a quantitative bottom-up proteomics analysis. Protein abundance was evaluated by Label-Free Quantitation (LFQ) to determine relative enrichment or loss of particular pilus proteins at either 68 °C or 58 °C. At both temperatures, the major pilin subunit PilA4 was identified as the most abundant protein component (Fig. S2a). The amount of PilA4 increased significantly at 58 °C, in line with the hyperpiliation phenotype [14]. The second most abundant protein was the uncharacterised protein TT_C1836; the relative abundance was also significantly increased at 58 °C.

110 To refine the identification of pilins, we performed gel based proteomic analysis (Fig. S2b,
111 Table S1). In order to increase the hyperpiliation phenotype, we further reduced the growth
112 temperature to 55 °C. At this temperature we could identify PilA4 and TT_C1836 as the most
113 abundant proteins in the lower molecular weight bands, likely representing the pilin
114 monomers. In contrast, at the optimal growth temperature of 68 °C, only PilA4 was identified
115 reliably. We questioned whether the two T4P were expressed due to differences in
116 temperature or growth phase. To quantify the abundance of different filaments, cells were
117 grown under different conditions and analysed in the electron microscope. Pili at both cell
118 poles were selected for 2D classification, which enables grouping of similar structures (Fig.
119 S3a). For cells grown on plates, both wide and narrow pili were present at a similar level,
120 whereas the ratio of the two was shifted towards the wider form for cells grown in liquid
121 medium. At 55 °C, only the total number of pili per cell increased, while the ratio between
122 wide and narrow pili was similar between the two temperatures (Fig. S3b).
123
124 To analyse the role of PilA4 and TT_C1836 in pilus assembly, we investigated the number of
125 wide and narrow pili per cell in deletion strains grown in liquid media to exponential phase
126 (Fig. S3c). PilA4 deficient cells (*pilA4::km*) were not able to assemble any pili reliably, whereas
127 TT_C1836 deficient cells (*TT_C1836::km*) were only defective in their ability to assemble
128 narrow pili. These findings suggest that PilA4 has a role in producing both pilus forms, while
129 TT_C1836 appears to be crucial for the formation of narrow pili only. However, these data do
130 not allow us to discriminate whether the proteins have structural roles in comprising the
131 filaments, or have a more functional role in their assembly mechanism.
132
133 ***High-resolution maps determine the 3D structure of both filaments***
134 In order to investigate the architecture and protein composition of T4P at high resolution,
135 both filaments were subjected to analysis by single particle cryoEM and helical reconstruction.
136 In our micrographs, the wide pili appeared very straight while the narrow pili showed a much
137 higher degree of curvature, up to 2 μm radius (arrowhead in Fig. S4A, B). Based on 2D classes
138 (Fig. S4c, d) we determined the helical parameters for the wide and the narrow pilus (Fig. S5a–
139 d, see methods section for details). The rise and twist of the wide pilus measured 9.33 Å and
140 92.5° respectively, and the narrow pilus had a rise of 11.30 Å and a twist of 84.3°. Helical
141 reconstruction [28] resulted in maps at 3.22 Å (wide) and 3.49 Å (narrow) (Fig. 2a, b, S5e, f). The
142 diameter of the wide fibre is 70 Å (Fig. 2a) and is roughly cylindrical. In contrast, the narrow
143 filament has a zigzag-like appearance in projection, owing to a 15 Å-wide groove that winds
144 through the fibre. The diameter at any position along the long axis of the fibre axis is therefore
145 only 45 Å (Fig. 2b). Both structures were in good agreement with the data obtained *in situ* by

146 cryoET (Fig. 1). A low-resolution structure of the T4P from *T. thermophilus* was previously
147 determined by cryoET and sub-tomogram averaging, with a diameter of ~3.5 nm [11]. It seems
148 likely that this conformation represents the narrower form of the pilus.
149
150 Both maps clearly resolved individual pilin monomers. The peptide backbone could be easily
151 traced throughout each subunit and large side chains were visible (Fig. 2c, d). The centre of
152 each filament is formed by a bundle of long N-terminal α-helices, as has been demonstrated
153 for other filaments [17,23–25,29]. In both maps, each α-helix is interrupted by an unfolded stretch
154 (brackets in Fig. 2c, d), a conserved feature observed in the N-terminal domains of all available
155 T4P structures. Interestingly, the unfolded region is significantly longer for the pilin comprising
156 the narrow filament, resulting in a longer N-terminal stalk. The outer regions of both filaments
157 are formed by globular domains consisting of β-strands, a typical hallmark of the T4P C-
158 terminal domain [30]. Whilst the C-terminal head domains of both pili are comprised of central
159 β-sheets, the domain size and the region linking to the N-terminal α-helix appear different.
160 These findings suggest that the two pili are not only distinct with regards to their helical
161 parameters, but also consist of different proteins.
162
163 As shown, we observe both filaments emerging from the T4P machinery (Fig. 1). This is
164 supported by previous studies showing that mutants defective in the PilQ secretin channel do
165 not extrude pili [27]. In addition, previous studies have shown that a mutant defective in the
166 assembly ATPase PilF is non-piliated [9]. This suggests that both pili are extruded by the same
167 assembly machinery. The aperture within the central channel of PilQ is of sufficient dimension
168 to accommodate either form (Fig. 2e, f).
169
170 ***Atomic models of T4P***
171 The resolution and quality of both maps allowed us to unambiguously build an atomic model
172 for each filament *ab initio* (Fig. 3a - f). Guided by our mass spectrometry results, the position
173 of large side chains and clear differences in the length of the polypeptide backbones, we were
174 able to identify PilA4 as the building block for the wide pilus and the previously
175 uncharacterised protein TT_C1836 as the subunit for the narrow filament. We now propose
176 that TT_C1836 be named PilA5, in keeping with *Thermus* nomenclature.
177
178 The N-terminal α-helix, including the unfolded stretch, is comprised of the first 54 (PilA4) or
179 53 amino acids (PilA5). In both proteins the helix is disrupted by an unfolded stretch around
180 the conserved Pro22 (Fig. 3c, d, S6). The stretch in PilA4 is 4 amino acids long as opposed to
181 10 amino acids long in PilA5. The region between the N-terminal α-helix and the C-terminal

182 β-sheet, the so-called glycosylation loop, ranges in PilA4 from amino acids 55 to 77, with a
183 two-turn α-helix comprising amino acids 61-67. The C-terminal region is an antiparallel four-
184 stranded β-sheet with the last strand facing towards the N-terminus followed by a loop that
185 ends on the β-sheet. A disulphide bond between Cys89, which is located in the second strand,
186 and the penultimate amino acid Cys124, likely stabilises the C-terminus (Fig. 3e). The
187 glycosylation loop in PilA5 spans amino acids 54 to 71, with amino acids 62 to 65 forming a
188 one-turn helix. The C-terminal β-sheet is composed of five strands, one more than observed
189 in PilA4. Due to the additional β-strand in PilA5, the last strand faces away from the N-
190 terminus of the protein. The C-terminus of PilA5 is located between the β-sheet, the
191 glycosylation loop and the long α-helix. A disulphide bond is formed between Cys60 in the
192 glycosylation loop and Cys88 in the third β-strand (Fig. 3f). Both pilins are highly hydrophobic
193 at the N-terminal part of the α-helix, and more hydrophilic on the surface of the globular
194 domain (Fig. 3g & h). The hydrophobic helices bundle and form the hydrophobic core of the
195 assembled filament. PilA4 has no net charge but the filament displays a distinctive positively
196 charged groove along the filament axis (Fig. 3i). In contrast, PilA5 has a total of 2 negative
197 charges per subunit which leads to a patch of negative charge winding around the filament
198 (Fig. 3j).
199
200 A network of cooperative interactions between pilin subunits holds the fibres together. Each
201 subunit has 6 (wide form) or 7 (narrow form) physical interaction partners in each direction
202 of the fibre (thus 12 or 14 total interaction partners) spread in side-by-side or top-to-bottom
203 directions (Fig. S7a, b). Most of the interactions involve a large portion of the N-terminal α-
204 helices within the hydrophobic core as well as the head domains. In the wide (PilA4) filament,
205 each subunit (subunit A) interacts with the N-termini that project down from the next two
206 subunits (B and C) above and from the subunits which are six and seven subunits above (G
207 and H). A second interaction takes place between the upper part of the α-helix in subunit A
208 and the glycosylation loop in subunit B (Fig. S7a). In the narrow (PilA5) filaments, subunit A
209 interacts via its α-helix with the N-termini of subunits B, C, F, G and H, while there is an
210 additional interaction between the upper part of the α-helix in subunit A with the
211 glycosylation loop in subunit B (Fig. S7b).
212
213 For both types of pili, the largest interaction interface is between subunits which are 3 or 4
214 subunits apart (subunit A with subunit D and E). Thus each pilin subunit has a large interaction
215 interface with 6 other subunits (B, D and E in Fig. S7a, b) and 6 or 8 smaller interaction sites
216 (C, G, H in Fig. S7a and C, G, H, F in Fig. S7b). Most interactions involve the hydrophobic
217 sidechains in the centre of the filament and appear to be nonspecific, likely allowing sliding

218 movements between the subunits when the filaments are stretched. This is in accordance
219 with the observation that pili can stretch up to threefold upon force [31]. In addition, PilA4
220 contains salt bridges between Asp53 in subunit A and Arg30 in subunit D, and between Glu48
221 in subunit A and Arg28 in subunit E. In contrast, PilA5 contains a single salt bridge between
222 Glu68 in subunit A and Arg23 in subunit D (Fig. S7c). The conserved Glu5 is likely required to
223 neutralise the positive charge of the N-terminus within the hydrophobic core of the filament
224 [4,32,33]. A salt bridge is also found between Glu5 and the N-terminus of the neighbouring subunit
225 in other T4P [23,24] . For both *T. thermophilus* fibres the distance between Glu5 and adjacent N-
226 termini is too far to form a salt bridge. Instead, Glu5 forms an intramolecular salt bridge to
227 the N-terminus in the same subunit (Fig. S7c). This was also modelled for the related *Klebsiella*
228 *oxytoca* pseudopilus [34].
229
230 ***Posttranslational modification***
231 Densities were observed in both EM maps that protrude into the solvent and cannot be
232 attributed to the polypeptide backbone and were too large to account for an amino acid side
233 chain (Fig. 4). Interestingly, these densities co-localised with serine residues and were similar
234 in appearance to previously published densities attributed to glycosylation sites [29,35,36]. We
235 suggest that these densities correspond to O-linked glycosylation, which is consistent with the
236 previous finding that the major pilin PilA4 of *T. thermophilus* is glycosylated [37]. Glycosylation
237 has also been observed in similar locations in the X-ray structure of *N. gonorrhoeae* type IV
238 pilin head domain (PDB: 2HI2) [16,17,38]. In PilA4, we found extra densities at 3 serine residues in
239 the glycosylation loop (Ser59, Ser66 and Ser71), while only one serine appeared to be
240 modified in PilA5 (Ser73). Interestingly the density was much more pronounced in PilA5 than
241 in PilA4. This may be due to a less flexible glycan moiety in PilA5, allowing for improved
242 resolution, or by a different composition of the sugar residues entirely. Glycosylation may
243 enhance temperature stability via additional hydrogen bonds, increase adhesive properties
244 (either to surfaces or to small molecules such as DNA) or act as recognition tags for cell-cell
245 communication [39].
246
247 ***The functional importance of two types of pili***
248 A key outstanding question pertains to the functional relevance of the two types of T4P.
249 To investigate this question, we performed various functional analyses on PilA4 and PilA5
250 deletion strains. We assessed cell lines without pili (*pilA4::km*), with wide pili only (*pilA5::km*),
251 or a mixed population of wide and narrow pili (wild type).
252

253 We analysed cellular motility by twitching assays at 68 °C and 55 °C. Wild-type cells formed
254 characteristic twitching zones of ~2 cm and ~1.2 cm in diameter, respectively. The mutants
255 *pilA4::km* and *pilA5::km* did not exhibit any twitching motility (Fig. 5a). Since the immotile
256 *pilA5*::km cells could still produce wide pili comprised of PilA4, we deduce that PilA5 is
257 required to promote cell movement. Cells lacking both types of pili in the *pilA4::km* mutant
258 were completely defective in natural transformation, in agreement with our former finding [40].
259 Transformation efficiency was only partially reduced in the *pilA5::km* mutant (~30%), which
260 expresses wide PilA4 pili (Fig. 5b). This corresponds to our previous finding that a *pilA5::km*
261 mutant is still transformable [40] and demonstrate that the narrow pili are dispensable for DNA
262 uptake.
263
264 In summary, we conclude that PilA4 has three known roles: it promotes pilus formation for
265 both wide and narrow filaments, it comprises the main structural element of the wide T4P,
266 and it plays a role in natural transformation. We determine two functions for PilA5: it forms
267 the basis of the narrow T4P and is a requirement for cell motility.
268
269
270 **Discussion**
271 We have determined the first cryoEM structures of T4P that have allowed atomic models to
272 be built *ab initio*. Moreover, we have discovered two distinct T4P filaments, which are
273 composed of different proteins. Our data provide compelling evidence that PilA5 is essential
274 for twitching motility and confirm the previous finding that PilA4 is involved in natural
275 transformation [40]. In addition, we find that PilA4 is essential for the assembly of both wide and
276 narrow pili. PilA4 may therefore play a crucial regulatory role, could initiate pilus formation,
277 or even form a capping structure. In many bacteria, minor pilins are thought to prime pilus
278 assembly by reducing the energy barrier to the extraction of pilins from the membrane [41]. In
279 *Thermus*, PilA4 may perform this role.
280
281 The unique functionality of PilA4 and PilA5 is hardcoded in their distinct structural features.
282 Both filaments follow the conserved T4P blueprint, encompassing a central bundle of
283 hydrophobic N-terminal α-helices and a hydrophilic C-terminal β-strand globular domain [39].
284 Structural variations in PilA4 and PilA5 determine distinct inter-subunit interactions, helical
285 parameters, mechanical properties, adhesiveness and binding affinity. Narrow pili comprised
286 of PilA5 are more flexible than those comprised of PilA4. In line with their predicted role in
287 twitching, narrow pili that can bend and flex would enable the filaments to curve from the
288 surface of cells to interact with surfaces, negotiate obstacles and increase the exploratory

289 range of the cell. Their overall net negative surface charge would enhance the adhesive
290 properties of the fibre and facilitate surface adhesion.
291
292 In accordance with the role of PilA4 in natural transformation, the surface of wide PilA4
293 filaments show a striking line of positively-charged residues along the long axis. We speculate
294 that these may be involved in binding the negatively charged DNA backbone. A double
295 stranded DNA molecule fits into a right-handed helical groove flanked by glycan residues. This
296 would allow interaction of the DNA backbone phosphates with positive charges in the PilA4
297 filament at regular intervals. Flanking glycans and negative charges may coordinate proper
298 DNA binding (Fig. 6). This suggestion is in good agreement with the well characterised roles of
299 T4P in DNA binding and uptake in *Neisseria*, and of DNA binding in *P. aeruginosa* [42,43]. Our
300 proposal is also consistent with that of Craig *et al,* who suggest that the positively charged
301 groove of gonoccocal T4P is wide enough to bind the negatively charged backbone of dsDNA
302 [17]. Interestingly, previous experiments have shown that pili are not solely important for
303 natural transformation. For example, a mutant defective in the PilF assembly ATPase was
304 impaired in piliation and was hypertransformable, and a mutant carrying a deletion in a
305 domain of the secretin PilQ was impaired in piliation but exhibited wildtype transformation
306 frequencies [10,44]. Taken together, we suggest that wide pili comprised of PilA4 may capture
307 DNA rather like a fishing net, thus improving the efficiency of DNA uptake by increasing the
308 local concentration of DNA near the outer membrane.
309
310 In evolutionary terms, bacteria appear to have reused the T4P blueprint to develop a system
311 that can assemble two different filaments with unique properties. This could enable tasks to
312 be performed more effectively and at reduced energy cost to the cell. It will now be interesting
313 to discover if this principle occurs in other bacterial species, and excitingly, will open avenues
314 to the development of vaccines or therapeutics targeting a particular T4P mechanism.
315
316
317 **Experimental procedures**
318 **Cultivation of organisms**
319 *T. thermophilus* HB27 was grown in TM^+ medium (8 g/l tryptone, 4 g/l yeast extract, 3 g/l NaCl,
320 0.6 mM $MgCl_2$, 0.17 mM $CaCl_2$) [45] at 55 °C, 58 °C or 68 °C. Antibiotics were added when
321 appropriate (kanamycin, 80 mg/ml; streptomycin, 100 mg/ml in solid medium (containing 2
322 % agar [w/vol]) or kanamycin, 60 mg/ml; streptomycin 100 mg/ml in liquid medium).
323 Disruption of *TT_C1836* and *pilA4* was performed by insertion of a kanamycin marker [27].
324

325 **Purification of pili**

326 *T. thermophilus* HB27 cells were grown for two days on TM^+ medium at 68 °C or three days at
327 55 °C.. Cells were scraped off and resuspended by pipetting and shaking in ethanolamine
328 buffer (0.15 M ethanolamine, pH 10.5). Cells were sedimented by centrifugation (16.200 *x g*,
329 1 h, 4 °C). The supernatant was gently mixed with saturated ammonium sulfate solution [10/1
330 (v/v)] and incubated on ice for 12 h. Pili were precipitated by centrifugation for 10 min (16,200
331 *x g*, 4 °C). The resulting pellet was washed twice with TBS buffer (50 mM Tris/HCl, 150 mM
332 NaCl, pH 7.5). The pellet was resuspended by incubation in distilled water for 4 h. 10x buffer
333 (500 mM Tris/HCl, 500 mM NaCl, 10 mM $CaCl_2$, 10 mM $MgCl_2$, pH 7.5) was added prior to
334 structural analyses.

335

336 **CryoET sample preparation and imaging**

337 Cubes of agar with growing *T. thermophilus* HB27 cells were cut out, placed into EDTA buffer
338 (20 mM Tris/HCl, 100 mM EDTA, pH 7.4) and gently agitated for 1 hour at room temperature.
339 Samples were mixed 1:1 with 10 nm protein A-gold (Aurion, Wageningen, The Netherlands)
340 as fiducial markers and glow-discharged R2/2 Cu 300 mesh holey carbon-coated support grids
341 (Quantifoil, Jena, Germany) were dipped into the solution. For analysis of isolated pili by
342 cryoET, preparations were mixed 1:1 with 10 nm protein A-gold fiducial markers and solutions
343 were gently pipetted onto the grids. All grids were blotted using Whatman 41 filter paper for
344 ~4 s in a humidified atmosphere and plunge-frozen in liquid ethane in a home-built device or
345 using a Vitrobot Mark IV (Thermo Fisher, Waltham, USA). Grids were maintained under liquid
346 nitrogen and transferred into the electron microscope at liquid nitrogen temperature.

347

348 Tomograms were typically collected from +60° to -60° at tilt steps of 2° and 5 - 7 µm
349 underfocus (whole cells), or at 3 µm underfocus (isolated pili), using either a Tecnai Polara,
350 Titan Krios (Thermo Fisher) or JEM-3200FSC (JEOL, Tokyo, Japan) microscope, all equipped
351 with field emission guns operating at 300 keV. All instruments were fitted with energy filters
352 and K2 Summit direct electron detector cameras (Gatan, Pleasanton, USA). Dose-fractionated
353 data (3-5 frames per projection image) were collected using Digital Micrograph (Gatan).
354 Magnifications varied depending on microscope; pixel sizes were within the range 3.8 – 4.2 Å.
355 The total dose per tomogram was < ~$140e^-/Å^2$. Tomograms were aligned using gold fiducial
356 markers and volumes reconstructed by weighted back-projection using the IMOD software
357 (Boulder Laboratory, Boulder, USA) [46]. Contrast was enhanced by non-linear anisotropic
358 diffusion (NAD) filtering in IMOD [47].

359

360 **Calculations of pilus diameter**

361 Slices through tomograms were analysed by drawing a plot profile of grey values in ImageJ [48],
362 which could be exported as a function of distance. Statistical analysis of pilus diameters was
363 conducted with a sample size of 8 tomograms containing ~60 isolated pili.
364
365 **Negative-stain electron microscopy**
366 Two microliters of purified pili were pipetted onto glow-discharged carbon-coated Cu 400
367 mesh support grids (Sigma-Aldrich) for 2 minutes. Grids were blotted with Whatman No 41
368 filter paper and stained with 5 % ammonium molybdate for 60 s. Images were recorded with
369 a Tecnai Spirit microscope (Thermo Fisher) operated at 120 keV and a OneView CMOS camera
370 (Gatan). Images were analysed for fibre quality, size, sample density and homogeneity using
371 EMAN2 [49]. For whole cell samples of *T. thermophilus*, either liquid culture was used directly or
372 some cells were carefully scraped off the plates and resuspended in TBS. If required, cells were
373 diluted in TBS. Negative staining was performed as described above. For the quantitative
374 analysis of number and type of pili per cell, filaments from each cell pole were counted and
375 helices of equal length were selected using e2helixboxer (EMAN2) and subsequently classified
376 in 2D using RELION [50]. The percentage of wide, narrow and unassigned pili was calculated
377 based on the number of particles in each class.
378
379 **CryoEM sample preparation and imaging of fibres**
380 Three microliters of isolated pilus suspension were pipetted onto a glow-discharged R2/2 Cu
381 300 mesh holey carbon-coated grids (Quantifoil). Grids were plunge frozen in liquid ethane
382 after blotting using a Vitrobot Mark IV (Thermo Fisher) and stored in liquid nitrogen. Cryo
383 images were collected with a Titan Krios microscope (Thermo Fisher) at the UK national
384 electron bio-imaging centre (eBIC), equipped with a field emission gun operating at 300 keV .
385 The microscope was fitted with K2 Summit direct electron detector and Quantum energy filter
386 (both Gatan, Pleasanton, USA). Dose-fractionated data were collected at 1.5 – 4 µm defocus
387 using EPU (Thermo Fisher). 3138 micrographs containing both forms of pili were collected as
388 40-frame movies, corresponding to 8 seconds at a frame rate of 1 frame for every 0.2 seconds.
389 The total dose was 48 electrons/$Å^2$ at a magnification of 130,000 x, corresponding to a pixel
390 size of 1.048 Å.
391
392 **Image processing, symmetry determination and helical reconstruction**
393 Drift correction was performed using UNBLUR [51]. Straight sections of thin and wide fibres were
394 boxed separately from the drift corrected images using the helixboxer function of EMAN2,
395 such that the filaments were centred in each rectangular box. Helical reconstruction was
396 performed using the boxed filaments and SPRING as follows [52]. Contrast transfer function

397 (CTF) correction was performed using CTFFIND [53]. In order to determine the helical
398 parameters of the wide filaments a subset of the boxed filaments were cut into small
399 segments of 373 Å (a multiple of the helical rise) with an 80 % overlap, yielding a total of 9576
400 segments, which were classed in 2D (Fig. S4a). Close examination of the segments indicated a
401 filament diameter of 75 Å. The calculated power spectrum from the total segments indicated
402 clear layer lines that could be indexed. A meridional reflection at approximately 9 Å and a
403 layer line of order 1 at approximately 36 Å indicated that there are approximately 4 subunits
404 per turn. The ninth layer was found to be of order 1, suggesting that the helix repeats exactly
405 after nine turns, with a non-integer number of subunits per turn. The
406 SEGMENTCLASSRECONSTRUCT module in SPRING on class averages was used to determine
407 the accurate helical symmetry (Fig. S5a). The suggested output was determined to be either
408 4.10 or 3.89 subunits in a helical pitch of 36.3 Å. In order to determine the helical parameters
409 for the narrow filaments a subset of the boxed filaments were cut into segments of 800 Å with
410 a step size of 330 Å and classed in 2D (Fig. S4b). The helical pitch could be determined directly
411 as 48.1 Å. A meridional reflection and thus a helical rise at 11.3 Å could be identified. These
412 parameters allow calculation of a helical rotation of 84.6° and 4.26 subunits per turn. The
413 SEGMENTCLASSRECONSTRUCT module in SPRING was again used to determine the accurate
414 helical symmetry (Fig. S5b). The suggested output was determined to be either 4.11, 4.14,
415 4.27 or 4.30 subunits with a helical pitch of 48.1 Å. 3D reconstruction was performed using
416 the above parameters by iterative projection matching and back projection as implemented
417 in the SEGMENTREFINE3D of SPRING, starting from a solid cylinder of 75 Å as a reference.
418 Examination of the Fourier transforms simulated from the reconstructed volume to that
419 experimentally calculated from fibres indicated that 3.89 subunits in a pitch of 36.3 Å
420 (accounting for a helical rise of 9.33 Å and a helical rotation of 92.5 degrees) is correct for the
421 wide filaments, and 4.27 subunits in a pitch of 48.1 Å (accounting for a helical rise of 11.26 Å
422 and a helical rotation of 84.3 degrees) is correct for the narrow filaments (Fig. S5c, d). For the
423 final maps 300 Å segments with a step size of three times the helical rise from 400 images
424 were extracted. Doubling the number of used images did not further increase the final
425 resolution. The calculated final maps were determined at 3.22 Å resolution from 98,415
426 asymmetric units for wide filaments, and 3.49 Å from 76,866 asymmetric units for narrow
427 filaments (Fig. S5e, f) using Fourier shell correlation (0.143 cut-off). For the final maps a B-
428 factor of -60 $Å^2$ was applied. Figures were drawn in Chimera, Coot and CCP4mg [54–56].

429

430 **Model building**

431 Atomic models for both forms of pili were built manually *de novo* in Coot. We assumed that
432 one of the two pili consists of the major pilin PilA4, which is 125 amino acids in length. The

433 backbone as well as all large side chain densities of PilA4 match the density map of the wider
434 form of the pilus. While tracing the backbone into the density maps it became apparent that
435 the subunits forming the narrower pili are ~10% smaller than the subunits of the wider pili.
436 Following the results of mass spectrometry and deletion experiments we modelled the second
437 most abundant protein, TT_C1836 (111 amino acids) into the density map of thin pili. The
438 backbone and visible side chains fit perfectly into the density map. The structure was
439 iteratively refined by Refmac5 [57] followed by manual rebuilding in Coot and ISOLDE [58]. The
440 final models contain all amino acid residues of the mature protein. The double stranded DNA
441 in Fig. 6 (based on PDB: 1bna) was modelled around the wide pilus using Chimera and Coot.
442
443 **Data deposition**
444 The cryo-EM maps were deposited in the Electron Microscopy Data Bank with accession codes
445 EMD-XXXX (wide pilus) and EMD-YYYY (narrow pilus). The structure coordinates of the atomic
446 models of the wide and the narrow pilus were deposited in the Protein Data Bank with
447 accession numbers WWWW and ZZZZ, respectively.
448
449 **Sequence Alignment**
450 Sequence alignment was performed using the PRALINE server [59] with the default settings
451 (weight matrix: BLOSSUM62, gap opening penalty: 12, gap extension penalty: 1).
452
453 **Mass spectrometry**
454 Purified pilus preparations were processed using a modified FASP workflow [60] as described
455 previously [61]. In brief, reduced and alkylated protein extracts were digested sequentially with
456 Lys-C and trypsin on Microcon-10 filters (Merck Millipore, # MRCPRT010 Ultracel YM-10).
457 Digested samples were desalted using ZipTips according to the manufacturer's instructions,
458 dried in a Speed-Vac and stored at -20 ^{o}C until LC/MS-MS analysis. Dried peptides were
459 dissolved in 5 % acetonitrile with 0.1 % formic acid, and subsequently loaded using a nano-
460 HPLC (Dionex U3000 RSLCnano) on reverse-phase columns (trapping column: particle size
461 3µm, C18, L=20mm; analytical column: particle size <2µm, C18, L=50cm; PepMap,
462 Dionex/Thermo Fisher). Peptides were eluted in gradients of water (buffer A: water with 5 %
463 v/v acetonitrile and 0.1 % formic acid) and acetonitrile (buffer B: 20 % v/v water and 80 % v/v
464 acetonitrile and 0.1 % formic acid). All LC-MS-grade solvents were purchased from Fluka.
465 Gradients were ramped from 4 % to 48 % B in 120 minutes at flow rates of 300 nl/min.
466 Peptides eluting from the column were ionised online using a Thermo nanoFlex ESI-source
467 and analysed in a Thermo "Q Exactive Plus" mass spectrometer. Mass spectra were acquired
468 over the mass range 350-1400m/z (Q Exactive Plus) and sequence information was acquired

469 by computer-controlled, data-dependent automated switching to MS/MS mode using
470 collision energies based on mass and charge state of the candidate ions.
471
472 Raw MS data were processed and analysed with MaxQuant [62] . In brief, spectra were matched
473 to the full 15 nalyse.org database (reviewed and non-reviewed, downloaded on the
474 13/05/2016) and a contaminant and decoy database. Precursor mass tolerance was set to 4.5
475 ppm, fragment ion tolerance to 20 ppm, with fixed modification of Cys residues
476 (carboxyamidomethylation +57.021) and variable modifications of Met residues (Ox +15.995),
477 Lys residues (Acetyl +42.011), Asn and Gln residues (Deamidation +0.984) and of N-termini
478 (carbamylation +43.006). Peptide identifications were calculated with FDR = 0.01, and
479 proteins with one peptide per protein included for subsequent analyses. Proteomics data
480 associated with this manuscript have been uploaded to PRIDE [63]. Anonymous reviewer access
481 is available upon request. Peptide intensities (label free quantitation) were analysed using
482 MaxQuant and Perseus [62]. Differential abundance of proteins (detected in at least 3 of 4
483 replicates in each condition) was analysed using a two-sided t test with a FDR of 0.01 and s0
484 = 0.05.
485
486 For gel-based MS, purified pili were separated by SDS-PAGE (Mini Protean TGX 4-15 %, Biorad,
487 Hercules, USA) and proteins were stained using Bio-Safe Coomassie Stain (Biorad, Hercules,
488 USA). Bands were cut out and analysed by MS at the University of Bristol Proteomics Facility.
489
490 **Twitching motility**
491 *T. thermophilus* HB27 strains were grown at 68 °C for 3 days and at 58 °C for 7 days under
492 humid conditions on minimal medium agar plates [10] containing 0.1 % bovine serum albumin.
493 Plates were then stained with Coomassie blue and cells washed off to reveal twitching zones.
494 The contrast has been inverted in the images.
495
496 **Natural transformation**
497 *T. thermophilus* wild-type, *pilA4::km* and *TT_C1836::km* mutants were cultured in TM^+ media
498 containing appropriate antibiotics for 24h at 68 °C, 150 rpm (New Brunswick Innova 42,
499 Eppendorf, Hamburg, Germany). These cultures were used to inoculate 10 ml TM^+ media (with
500 appropriate antibiotics) to a starting OD600 = 0.2 and incubated until OD600 = 0.5 was
501 reached. 30 µl of the cultures were transferred into 370 µl prewarmed TM^+ medium, and 10
502 µg genomic DNA from a spontaneous streptomycin-resistant HB27 mutant was added (HB27
503 Strep). The cultures were incubated for 30 min at 68 °C, 150 rpm. These were subsequently

504 diluted (400 µl in 3 ml TM^+) and incubated for an additional 3 h at 68 °C, 150rpm.
505 Transformations were plated in suitable dilutions onto TM^+ agar plates containing 100 µg/ml
506 streptomycin to determine the number of transformants. The number of viable cells was
507 determined by plating on TM^+ agar plates lacking streptomycin. Following incubation for 2
508 days at 68°C, colonies were counted. The transformation efficiency was calculated as the
509 number of transformations per number of living cells.
510

511 **Acknowledgements**

512 We thank Werner Kühlbrandt and Deryck Mills for their support at the MPI of Biophysics in
513 Frankfurt, and Carsten Sachse for indispensable assistance using SPRING and feedback on early
514 versions of this manuscript. We thank Mathew McLaren for maintenance of the EM facility in
515 Exeter and we acknowledge access and support of the GW4 Facility for High-Resolution
516 Electron Cryo-Microscopy, funded by the Wellcome Trust (202904/Z/16/Z and 206181/Z/17/Z)
517 and BBSRC (BB/R000484/1). We acknowledge Diamond for access and support of the cryoEM
518 facilities at the UK national electron bio-imaging centre (eBIC), proposal EM18258, funded by
519 the Wellcome Trust, MRC and BBSRC. We thank Kate Heesom (University of Bristol Proteomics
520 Facility), Imke Wüllenweber and Fiona Rupprecht (MPI for Biophysics) for MS experiments.
521 We acknowledge the BBSRC (BB/R008639/1), Max-Planck-Society, the University of Exeter
522 and the Deutsche Forschungsgemeinschaft (AV 9/6-2) for funding.
523

524 **Author contributions**

525 Major contributions to (i) the conception or design of the study (AN, MS, RS, BD, BA, VAMG)
526 (ii) the acquisition, analysis, or interpretation of the data (AN, MS, RS, KK, KS, JDL, BD, BA,
527 VAMG); and (iii) writing of the manuscript (AN, MS, BD, VAMG). All authors commented on
528 the manuscript.
529

530 **Conflict of interest**

531 The authors declare no conflict of interest.

532 **References**

533 1. Hobbs, M. & Mattick, J. S. Common components in the assembly of type 4 fimbriae,
534 DNA transfer systems, filamentous phage and protein-secretion apparatus: a general
535 system for the formation of surface-associated protein complexes. *Mol. Microbiol.*
536 (1993). doi:10.1111/j.1365-2958.1993.tb01949.x
537 2. Kaiser, D. Bacterial motility: How do pili pull? *Current Biology* (2000).
538 doi:10.1016/S0960-9822(00)00764-8
539 3. Averhoff, B. & B., A. Shuffling genes around in hot environments: The unique DNA
540 transporter of Thermus thermophilus. in *FEMS microbiology reviews* **33**, 611–626
541 (2009).
542 4. Strom, M. S. & Lory, S. Amino acid substitutions in pilin of Pseudomonas aeruginosa.
543 Effect on leader peptide cleavage, amino-terminal methylation, and pilus assembly. *J.*
544 *Biol. Chem.* (1991).
545 5. Paetzel, M., Dalbey, R. E. & Strynadka, N. C. J. Crystal structure of a bacterial signal
546 peptidase apoenzyme. Implications for signal peptide binding and the Ser-Lys dyad
547 mechanism. *J. Biol. Chem.* (2002). doi:10.1074/jbc.M110983200
548 6. Karuppiah, V., Collins, R. F., Thistlethwaite, A., Gao, Y. & Derrick, J. P. Structure and
549 assembly of an inner membrane platform for initiation of type IV pilus biogenesis.
550 *Proc. Natl. Acad. Sci. U. S. A.* **110**, E4638-47 (2013).
551 7. Kruse, K., Salzer, R. & Averhoff, B. The traffic ATPase PilF interacts with the inner
552 membrane platform of the DNA translocator and type IV pili from
553 Thermus thermophilus. *FEBS Open Bio* (2019). doi:10.1002/2211-5463.12548
554 8. Rose, I. *et al.* Identification and characterization of a unique, zinc-containing
555 transport ATPase essential for natural transformation in Thermus thermophilus
556 HB27. *Extremophiles* (2011). doi:10.1007/s00792-010-0343-2
557 9. Salzer, R., Joos, F. & Averhoff, B. Type IV pilus biogenesis, twitching motility, and DNA
558 uptake in Thermus thermophilus: Discrete roles of antagonistic ATPases PilF, PilT1,
559 and PilT2. *Appl. Environ. Microbiol.* **80**, 644–652 (2014).
560 10. Burkhardt, J., Vonck, J., Langer, J. D., Salzer, R. & Averhoff, B. Unusual N-terminal
561 ααβαββα fold of PilQ from Thermus thermophilus mediates ring formation and is
562 essential for piliation. *J. Biol. Chem.* **287**, 8484–8494 (2012).
563 11. Gold, V. A. M., Salzer, R., Averhoff, B. & Kühlbrandt, W. Structure of a type IV pilus
564 machinery in the open and closed state. *Elife* **4**, (2015).
565 12. Salzer, R. *et al.* Topology and structure/function correlation of ring-and gate-forming
566 domains in the dynamic secretin complex of thermus thermophilus. *J. Biol. Chem.*
567 **291**, (2016).

568 13. D'Imprima, E. *et al.* Cryo-EM structure of the bifunctional secretin complex of
569 Thermus thermophilus. *Elife* (2017). doi:10.7554/elife.30483
570 14. Salzer, R., Kern, T., Joos, F. & Averhoff, B. Environmental factors affecting the
571 expression of type IV pilus genes as well as piliation of Thermus thermophilus. *FEMS*
572 *Microbiol. Lett.* (2014). doi:10.1111/1574-6968.12506
573 15. Chang, Y.-W. W. *et al.* Architecture of the type IVa pilus machine. *Science (80-.).* **351**,
574 aad2001 (2016).
575 16. Parge, H. E. *et al.* Structure of the fibre-forming protein pilin at 2.6 Å resolution.
576 *Nature* (1995). doi:10.1038/378032a0
577 17. Craig, L. *et al.* Type IV Pilus Structure by Cryo-Electron Microscopy and
578 Crystallography: Implications for Pilus Assembly and Functions. *Mol. Cell* **23**, 651–662
579 (2006).
580 18. Fukakusa, S. *et al.* Structure of the CFA/III major pilin subunit CofA from human
581 enterotoxigenic Escherichia coli determined at 0.90 Å resolution by sulfur-SAD
582 phasing. *Acta Crystallogr. Sect. D Biol. Crystallogr.* (2012).
583 doi:10.1107/S0907444912034464
584 19. Kolappan, S., Roos, J., Yuen, A. S. W., Pierce, O. M. & Craig, L. Structural
585 characterization of CFA/III and longus type IVb Pili from enterotoxigenic Escherichia
586 coli. *J. Bacteriol.* (2012). doi:10.1128/JB.00282-12
587 20. Gorgel, M. *et al.* High-resolution structure of a type IV pilin from the metal-reducing
588 bacterium Shewanella oneidensis. *BMC Struct. Biol.* (2015). doi:10.1186/s12900-015-
589 0031-7
590 21. Piepenbrink, K. H. *et al.* Structural diversity in the type IV Pili of multidrug-resistant
591 acinetobacter. *J. Biol. Chem.* (2016). doi:10.1074/jbc.M116.751099
592 22. Karuppiah, V., Thistlethwaite, A. & Derrick, J. P. Structures of type IV pilins from
593 Thermus thermophilus demonstrate similarities with type II secretion system
594 pseudopilins. *J. Struct. Biol.* (2016). doi:10.1016/j.jsb.2016.08.006
595 23. Kolappan, S. *et al.* Structure of the neisseria meningitidis type IV pilus. *Nat. Commun.*
596 1–12 (2016). doi:10.1038/ncomms13015
597 24. Wang, F. *et al.* Cryoelectron Microscopy Reconstructions of the Pseudomonas
598 aeruginosa and Neisseria gonorrhoeae Type IV Pili at Sub-nanometer Resolution.
599 *Structure* **25**, 1423-1435.e4 (2017).
600 25. Bardiaux, B. *et al.* Structure and Assembly of the Enterohemorrhagic Escherichia coli
601 Type 4 Pilus. *Structure* (2019). doi:10.1016/j.str.2019.03.021
602 26. Schwarzenlander, C., Haase, W. & Averhoff, B. The role of single subunits of the DNA
603 transport machinery of Thermus thermophilus HB27 in DNA binding and transport.

604 *Environ. Microbiol.* **11**, 801–808 (2009).
605 27. Friedrich, A., Prust, C., Hartsch, T., Henne, A. & Averhoff, B. Molecular analyses of the
606 natural transformation machinery and identification of pilus structures in the
607 extremely thermophilic bacterium Thermus thermophilus strain HB27. *Appl. Environ.*
608 *Microbiol.* **68**, 745–755 (2002).
609 28. Fromm, S. A. & Sachse, C. Cryo-EM Structure Determination Using Segmented Helical
610 Image Reconstruction. in *Methods in Enzymology* (2016).
611 doi:10.1016/bs.mie.2016.05.034
612 29. Daum, B. *et al.* Structure and in situ organisation of the pyrococcus furiosus
613 archaellum machinery. *Elife* **6**, (2017).
614 30. Craig, L. & Li, J. Type IV pili: paradoxes in form and function. *Current Opinion in*
615 *Structural Biology* **18**, 267–277 (2008).
616 31. Biais, N., Higashi, D. L., Brujic, J., So, M. & Sheetz, M. P. Force-dependent
617 polymorphism in type IV pili reveals hidden epitopes. *Proc. Natl. Acad. Sci. U. S. A.*
618 **107**, 11358–63 (2010).
619 32. Aas, F. E. *et al.* Substitutions in the N-terminal alpha helical spine of Neisseria
620 gonorrhoeae pilin affect Type IV pilus assembly, dynamics and associated functions.
621 *Mol. Microbiol.* (2007). doi:10.1111/j.1365-2958.2006.05482.x
622 33. Li, J., Egelman, E. H. & Craig, L. Structure of the Vibrio cholerae Type IVb pilus and
623 stability comparison with the Neisseria gonorrhoeae Type IVa pilus. *J. Mol. Biol.* **418**,
624 47–64 (2012).
625 34. Campos, M., Nilges, M., Cisneros, D. A. & Francetic, O. Detailed structural and
626 assembly model of the type II secretion pilus from sparse data. *Proc. Natl. Acad. Sci.*
627 (2010). doi:10.1073/pnas.1001703107
628 35. Poweleit, N. *et al.* CryoEM structure of the Methanospirillum hungatei archaellum
629 reveals structural features distinct from the bacterial flagellum and type IV pili. *Nat.*
630 *Microbiol.* **2**, 16222 (2016).
631 36. Meshcheryakov, V. A. *et al.* High-resolution archaellum structure reveals a conserved
632 metal-binding site. *EMBO Rep.* (2019). doi:10.15252/embr.201846340
633 37. Rumszauer, J., Schwarzenlander, C. & Averhoff, B. Identification, subcellular
634 localization and functional interactions of PilMNOWQ and PilA4 involved in
635 transformation competency and pilus biogenesis in the thermophilic bacterium
636 Thermus thermophilus HB27. *FEBS J.* **273**, 3261–3272 (2006).
637 38. Marceau, M., Forest, K., Béretti, J. L., Tainer, J. & Nassif, X. Consequences of the loss
638 of O-linked glycosylation of meningococcal type IV pilin on piliation and pilus-
639 mediated adhesion. *Mol. Microbiol.* (1998). doi:10.1046/j.1365-2958.1998.00706.x

640 39. Daum, B. & Gold, V. Twitch or swim: towards the understanding of prokaryotic
641 motion based on the type IV pilus blueprint. *Biol. Chem.* (2018). doi:10.1515/hsz-
642 2018-0157
643 40. Friedrich, A., Rumszauer, J., Henne, A. & Averhoff, B. Pilin-like proteins in the
644 extremely thermophilic bacterium Thermus thermophilus HB27: Implication in
645 competence for natural transformation and links to type IV pilus biogenesis. *Appl.*
646 *Environ. Microbiol.* **69**, 3695–3700 (2003).
647 41. Cisneros, D. A., Bond, P. J., Pugsley, A. P., Campos, M. & Francetic, O. Minor
648 pseudopilin self-assembly primes type II secretion pseudopilus elongation. *EMBO J.*
649 (2012). doi:10.1038/emboj.2011.454
650 42. Van Schaik, E. J. *et al.* DNA binding: A novel function of Pseudomonas aeruginosa type
651 IV pili. *J. Bacteriol.* (2005). doi:10.1128/JB.187.4.1455-1464.2005
652 43. Hamilton, H. L. & Dillard, J. P. Natural transformation of Neisseria gonorrhoeae: From
653 DNA donation to homologous recombination. *Molecular Microbiology* (2006).
654 doi:10.1111/j.1365-2958.2005.04964.x
655 44. Kruse, K., Salzer, R., Joos, F. & Averhoff, B. Functional dissection of the three N-
656 terminal general secretory pathway domains and the Walker motifs of the traffic
657 ATPase PilF from Thermus thermophilus. *Extremophiles* (2018). doi:10.1007/s00792-
658 018-1008-9
659 45. Oshima, T. & Imahori, K. Description of Thermus thermophilus (Yoshida and Oshima)
660 comb. nov., a Nonsporulating Thermophilic Bacterium from a Japanese Thermal Spa.
661 *Int. J. Syst. Bacteriol.* (1974). doi:10.1099/00207713-24-1-102
662 46. Kremer, J. R., Mastronarde, D. N. & McIntosh, J. R. Computer visualization of three-
663 dimensional image data using IMOD. *J. Struct. Biol.* (1996).
664 doi:10.1006/jsbi.1996.0013
665 47. Frangakis, A. S. & Hegerl, R. Noise reduction in electron tomographic reconstructions
666 using nonlinear anisotropic diffusion. *J. Struct. Biol.* (2001).
667 doi:10.1006/jsbi.2001.4406
668 48. Schneider, C. A., Rasband, W. S. & Eliceiri, K. W. NIH Image to ImageJ: 25 years of
669 image analysis. *Nat. Methods* (2012).
670 49. Tang, G. *et al.* EMAN2: an extensible image processing suite for electron microscopy.
671 *J. Struct. Biol.* (2007). doi:10.1016/j.jsb.2006.05.009
672 50. Scheres, S. H. W. RELION: Implementation of a Bayesian approach to cryo-EM
673 structure determination. *J. Struct. Biol.* (2012). doi:10.1016/j.jsb.2012.09.006
674 51. Grant, T. & Grigorieff, N. Measuring the optimal exposure for single particle cryo-EM
675 using a 2.6 Å reconstruction of rotavirus VP6. *Elife* (2015). doi:10.7554/elife.06980

676 52. Desfosses, A., Ciuffa, R., Gutsche, I. & Sachse, C. SPRING - An image processing
677 package for single-particle based helical reconstruction from electron
678 cryomicrographs. *J. Struct. Biol.* (2014). doi:10.1016/j.jsb.2013.11.003
679 53. Mindell, J. A. & Grigorieff, N. Accurate determination of local defocus and specimen
680 tilt in electron microscopy. *J. Struct. Biol.* (2003). doi:10.1016/S1047-8477(03)00069-
681 8
682 54. Pettersen, E. F. *et al.* UCSF Chimera--a visualization system for exploratory research
683 and analysis. *J. Comput. Chem.* (2004). doi:10.1002/jcc.20084
684 55. Emsley, P. & Cowtan, K. Coot: Model-building tools for molecular graphics. *Acta*
685 *Crystallogr. Sect. D Biol. Crystallogr.* (2004). doi:10.1107/S0907444904019158
686 56. McNicholas, S., Potterton, E., Wilson, K. S. & Noble, M. E. M. Presenting your
687 structures: The CCP4mg molecular-graphics software. *Acta Crystallogr. Sect. D Biol.*
688 *Crystallogr.* (2011). doi:10.1107/S0907444911007281
689 57. Brown, A. *et al.* Tools for macromolecular model building and refinement into
690 electron cryo-microscopy reconstructions. *Acta Crystallogr. Sect. D Biol. Crystallogr.*
691 (2015). doi:10.1107/S1399004714021683
692 58. Croll, T. I. ISOLDE : a physically realistic environment for model building into low-
693 resolution electron-density maps . *Acta Crystallogr. Sect. D Struct. Biol.* (2018).
694 doi:10.1107/s2059798318002425
695 59. Heringa, J. Two strategies for sequence comparison: Profile-preprocessed and
696 secondary structure-induced multiple alignment. *Comput. Chem.* (1999).
697 doi:10.1016/S0097-8485(99)00012-1
698 60. Wiśniewski, J. R., Zougman, A., Nagaraj, N. & Mann, M. Universal sample preparation
699 method for proteome analysis. *Nat. Methods* (2009). doi:10.1038/nmeth.1322
700 61. Schanzenbächer, C. T., Sambandan, S., Langer, J. D. & Schuman, E. M. Nascent
701 Proteome Remodeling following Homeostatic Scaling at Hippocampal Synapses.
702 *Neuron* (2016). doi:10.1016/j.neuron.2016.09.058
703 62. Tyanova, S., Temu, T. & Cox, J. The MaxQuant computational platform for mass
704 spectrometry-based shotgun proteomics. *Nat. Protoc.* (2016).
705 doi:10.1038/nprot.2016.136
706 63. Vizcaíno, J. A. *et al.* 2016 update of the PRIDE database and its related tools. *Nucleic*
707 *Acids Res.* (2016). doi:10.1093/nar/gkv1145
708

709 **Figures**

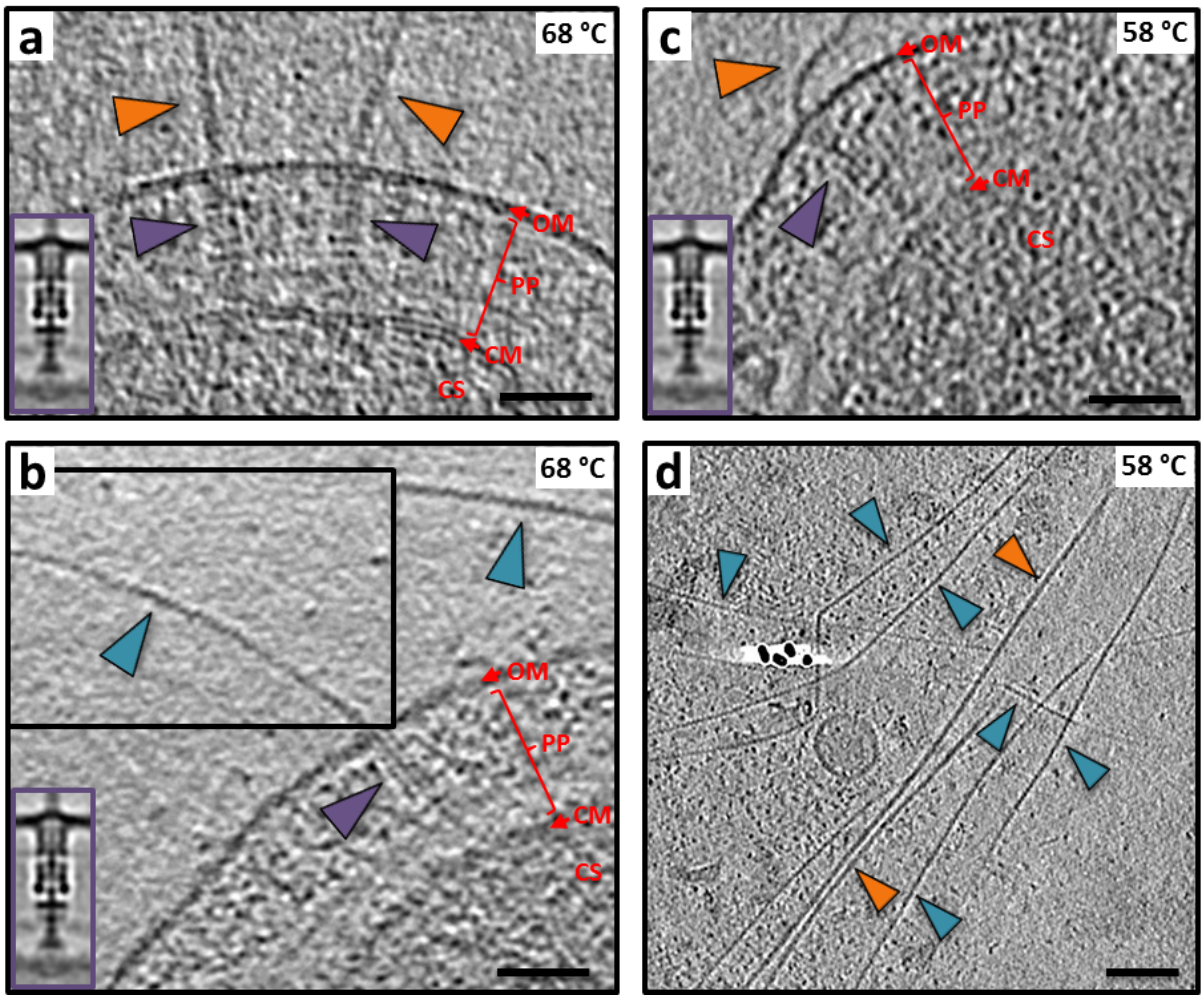

710

711 **Fig. 1: The T4P machinery assembles two types of pilus**

712 **a, b,** Tomographic slices through *T. thermophilus* cells grown at 68 °C show both wide (orange
713 arrowheads) and narrow (teal arrowheads) pili emerging from the T4P machinery (purple
714 arrowheads). The pilus emerges from the cell at an acute angle in (**b**), thus the tomographic
715 volume has been rotated to align with the T4P machinery for visualisation (upper inset box).
716 **c,** Tomographic slice through a *T. thermophilus* cell grown at 58 °C shows a wide pilus (orange
717 arrowhead) emerging from the T4P machinery (purple arrowhead).
718 **d,** Tomographic slice of an area containing many pili from a cell preparation grown at 58 °C.
719 Both wide (orange arrowheads) and narrow pili (teal arrowheads) are visible. Purple insets in
720 **a-c** show the subtomogram average of the T4P machinery (EMD-3023) [11]. OM, outer
721 membrane; PP, periplasm; CM, cytoplasmic membrane; CS, Cytosol. Scale bars, 50 nm.

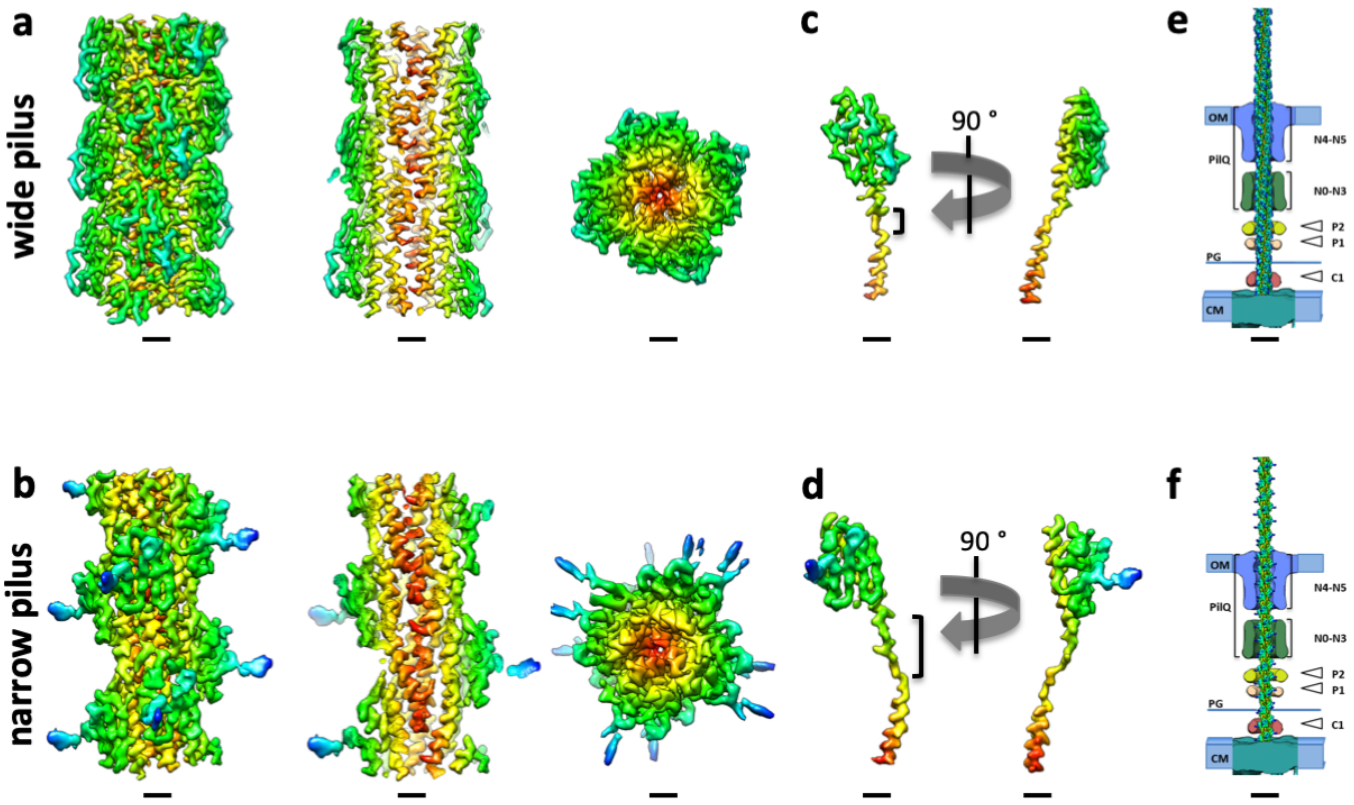

723 **Fig. 2: Helical reconstruction of *Tth*HB27 pili**

724 **a, b,** Side views, cross sections and top views of the density maps of the wide (**a**) and narrow
725 (**b**) pilus fibres. Coloured by cylinder radius from red (centre) to blue (periphery). Scale bars,
726 10 Å.

727 **c, d,** A single subunit of the wide (**c**) and narrow (**d**) pilus segmented from the maps in **a** and
728 **b**. The brackets show the melted stretch in the N-terminal α-helix. Scale bars, 10 Å.

729 **e, f,** Pilus filaments docked into the subtomogram average of the open state of the T4P
730 machinery (EMD-3023) [11]. Domains of the secretin PilQ (blue and green; N0-N5), with
731 unassigned protein densities P2 (yellow), P1 (orange) and C1 (red) are shown. OM, outer
732 membrane; PG, peptidoglycan; CM, cytoplasmic membrane. Scale bars, 10 nm.

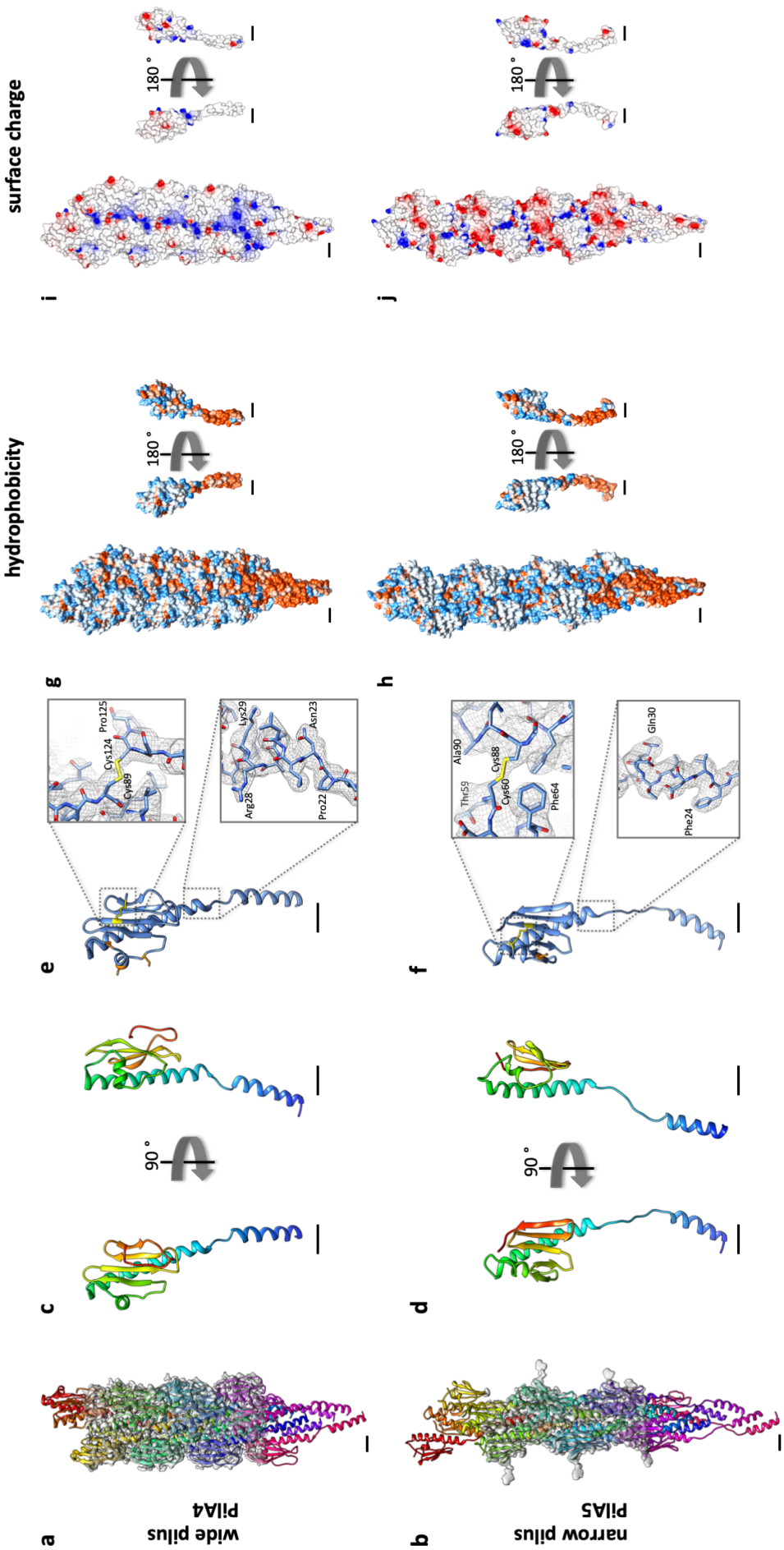

733 **Fig. 3: Molecular models of wide and narrow pili**

a, b, Molecular models of short sections of filaments (15 subunits each) with the corresponding EM density maps. **a,** wide pilus comprised of PilA4; **b,** narrow pilus comprised of PilA5. Scale bars, 10 Å.

c, d, Ribbon representation of a single PilA4 (**c**) and PilA5 (**d**) subunit. N-terminus blue, C-terminus red. Scale bars, 10 Å.

e, f, Ribbon representation of a single PilA4 (**e**) and PilA5 (**f**) subunit with selected sidechains shown. Yellow, disulphide bond; orange, serines with posttranslational modification. Insets show details of the molecular model within the EM density map. Top insets, disulphide bond; bottom insets, side chain densities. Scale bars, 10 Å.

g, h, Hydrophobicity of PilA4 (**g**) and PilA5 (**h**) filaments (left) and single subunits (right). Hydrophobic (red) and hydrophilic (blue) residues are shown. Scale bars, 10 Å.

i, j, Electrostatic surface charge of PilA4 (**i**) and PilA5 (**j**) filaments (left) and single subunits (right). Negative charges (red) and positive charges (blue) are shown. Scale bars, 10 Å.

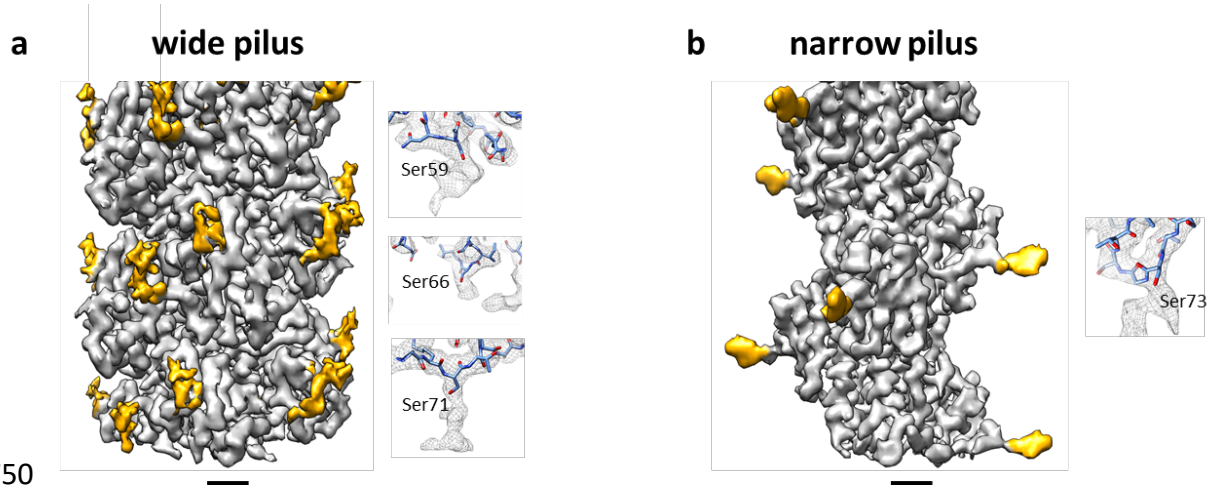

Fig. 4: Post-translational modification

a, b, Surface representation of the EM maps of the wide (**a**) and narrow (**b**) pilus showing the protein model (grey) and densities that protrude into the solvent and could not be attributed to the polypeptide backbone or an amino acid side chain. These are most likely glycans (yellow). Insets show close-ups of large unassigned densities near serine residues. Scale bars, 10 Å.

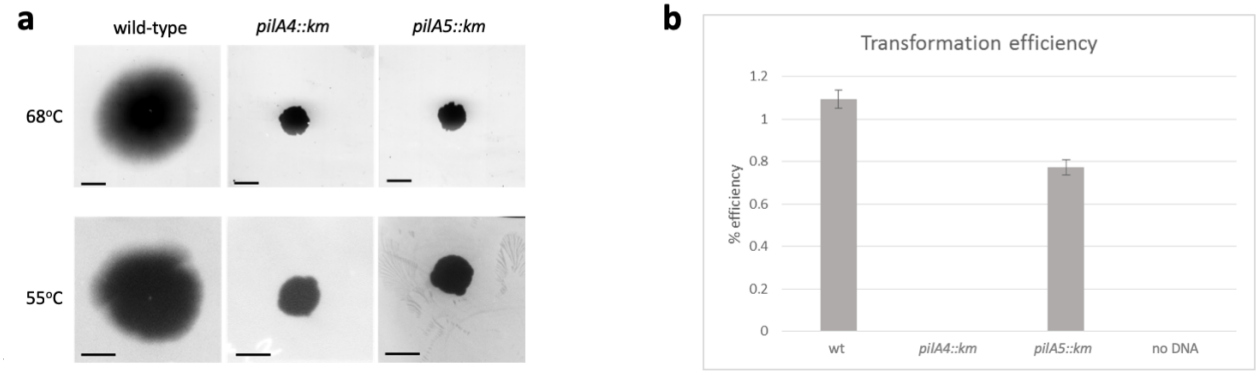

Fig. 5: Functional characterisation of *T. thermophilus* mutants

a, Twitching motility of *T. thermophilus* HB27 strains. Only wild-type cells show twitching. Scale bars = 0.5 cm.

b, Natural transformation efficiency of *T. thermophilus* HB27 strains.

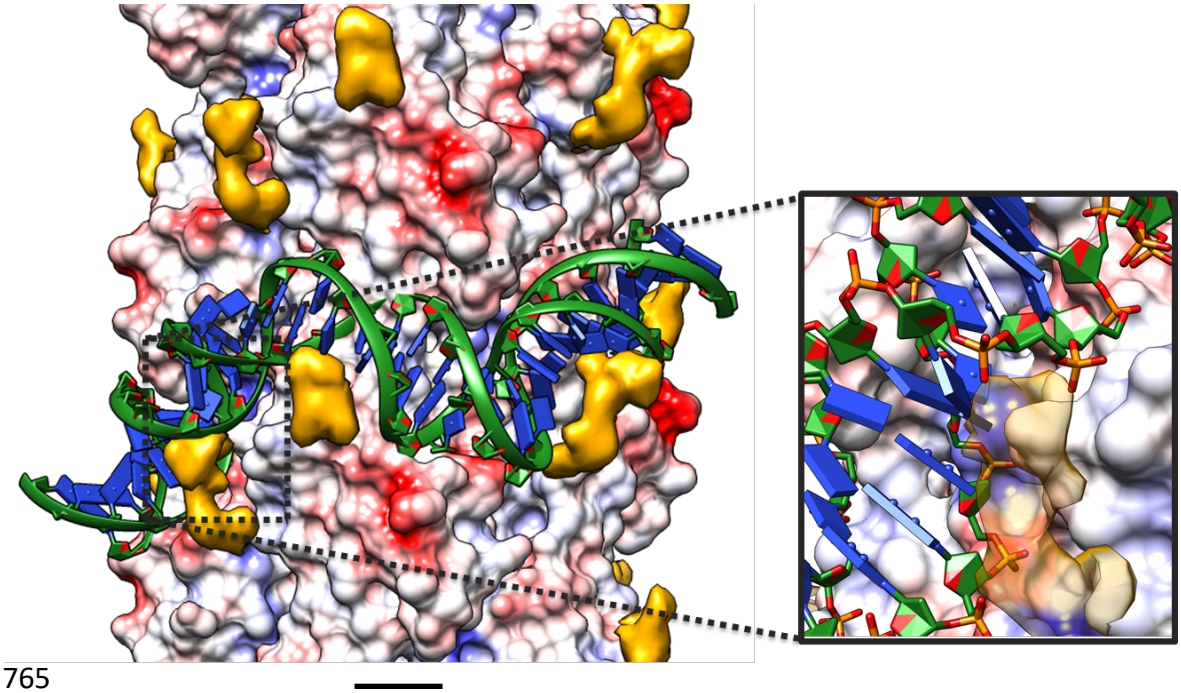

Fig. 6: Proposed DNA binding to wide pili

A double stranded DNA molecule (green) is modelled around a wide pilus shown in surface charge representation (negative charges, red; positive charges, blue). The DNA backbone fits neatly into the positively charged groove of the PilA4 filament (inset). Post-translational modifications are shown in yellow (transparent yellow in inset). Scale bar, 10 Å.